Experimental investigation of aerodynamic hysteresis using a 5-DoF wind tunnel manoeuvre rig

Z. Gong[*]

Nanjing University of Aeronautics and Astronautics, College of Aerospace Engineering, Nanjing, China

S. Araujo-Estrada[†] and M.H. Lowenberg[‡] and S.A. Neild[§]

University of Bristol, Queens Building, University Walk, Bristol, BS8 1TR, UK

M.G. Goman[¶]

De Montfort University, Faculty of Technology, The Gateway, Leicester, LE1 9BH, UK

The high incidence aerodynamics of a lightweight jet trainer aircraft model has been investigated using a novel five degree-of-freedom (DoF) dynamic manoeuvre rig, recently updated with improved actuation and data acquisition systems, in the $7' \times 5'$ closed-section low-speed wind tunnel at the University of Bristol. The major focus was to identify the nonlinear and unsteady aerodynamic characteristics specific to the stall region and which affect free-to-move aircraft model behaviour. First, the unstable equilibrium states in the limit cycle regions were stabilized, and so observed, over a wide range of angles of attack using a simple elevator feedback control law based on pitch angle and pitch-rate sensor measurements.

Tests with two degrees-of-freedom, namely the aircraft model and rig arm pitch angles, revealed the existence of static hysteresis in the normal force acting on the aircraft model in the stall region. Unlocking the aircraft model in roll and yaw accompanied by feedback stabilization of the lateral-directional modes of motion demonstrated onset of asymmetric aerodynamic rolling and yawing moments in this four degree-of-freedom configuration. This observation implicitly indicates a link between the static hysteresis in the normal aerodynamic force with an onset of aerodynamic asymmetry. The experimental results show the efficiency of the updated multi-degree-of-freedom actively controlled manoeuvre rig in providing insight into complicated aerodynamic effects within the stall region.

Nomenclature

C_L =   aircraft model lift coefficient

---

[*]Lecturer, Dept. of Aerospace Engineering.

[†]Research Associate, Dept. of Aerospace Engineering.

[‡]Professor of Flight Dynamics, Dept. of Aerospace Engineering, Senior Member AIAA.

[§]Professor in Nonlinear Structural Dynamics, Dept. of Mechanical Engineering.

[¶]Professor of Dynamics, School of Engineering and Sustainable Development, Senior Member AIAA.

C_{L_c} = rig arm compensator lift coefficient

C_l = aircraft model rolling moment coefficient

C_{l_β} = derivative of C_l with respect to sideslip angle (effective dihedral)

$C_{l_{\delta a}}$ = derivative of C_l with respect to aileron angle

C_N = aircraft model normal force coefficient

C_{Nc} = compensator normal force coefficient

$C_{Nc_{\theta_a}}$ = derivative of C_{Nc} with respect to rig arm pitch angle

$C_{Nc_{\delta_{ec}}}$ = derivative of C_{Nc} with respect to compensator elevator angle

C_n = aircraft model yawing moment coefficient

C_{n_β} = derivative of C_n with respect to sideslip angle

$C_{n_{\delta r}}$ = derivative of C_n with respect to rudder angle

k_{q_a} = rig arm pitch rate gain

k_q = aircraft model pitch rate gain

k_p = aircraft model roll rate gain

k_r = aircraft model yaw rate gain

k_θ = aircraft model pitch angle proportional gain

k_ϕ = aircraft model roll angle proportional gain

k_ψ = aircraft model yaw angle proportional gain

M = mass of the combined arm and aircraft model

p = aircraft model roll rate

q = aircraft model pitch rate

q_a = rig arm pitch rate

$\bar{q}$ = dynamic pressure

r = aircraft model yaw rate

S = aircraft model reference wing area

S_c = rig compensator reference area

X_{CG} = location of the centre of gravity (CG) of the rig arm, compensator and aircraft model from vertical strut gimbal centre in horizontal direction when $\theta_a = 0$

X_m = aircraft model lift arm measured from vertical strut gimbal

X_c = compensator lift arm measured from vertical strut gimbal

Z_{CG} = location of the centre of gravity (CG) of the rig arm, compensator and aircraft model from vertical strut gimbal centre in vertical direction when $\theta_a = 0$

α	=	aircraft model angle of attack
β	=	aircraft model sideslip angle
δ_a	=	aircraft model aileron angle
δ_{a_d}	=	aircraft model aileron demand input
δ_e	=	aircraft model elevator angle
δ_{e_d}	=	aircraft model elevator demand input
δ_{ec}	=	compensator elevator angle
δ_{ec_d}	=	compensator elevator demand input
δ_r	=	aircraft model rudder angle
δ_{r_d}	=	aircraft model rudder demand input
ϕ	=	aircraft model roll angle
ϕ_s	=	aircraft model trim roll angle
ψ	=	aircraft model yaw angle
ψ_s	=	aircraft model trim yaw angle
θ	=	aircraft model pitch angle
θ_a	=	rig arm pitch angle
CFD	=	Computational Fluid Dynamics
CG	=	Centre of Gravity
DoF	=	Degree-of-Freedom

I. Introduction

The deterioration of aerodynamic characteristics at high angles of attack due to separated flow conditions results in various types of loss of control and dynamic instability. These can limit manoeuvrability for fighter aircraft and affect flight safety of transport aeroplanes.

Wind tunnel testing techniques are traditionally used for characterization of aerodynamic loads for aircraft design, aerodynamic modelling and flight simulation. Various wind tunnel rigs are used for measuring aerodynamic forces and moments in static, forced-oscillation and rotary balance tests. The aerodynamic data obtained at high angles of attack are less reliable than at low to moderate incidence due to high sensitivity of separated flow to wind tunnel test conditions, such as the Reynolds number, flow turbulence, level of aeroelastic vibrations, and imperfection of wind tunnel flow and aircraft model geometry. Data obtained in different wind tunnels for the same aircraft model may differ significantly under high angle of attack conditions [1]. Research is needed to understand the complex flow phenomena due to flow separation in the stall region within the flight envelope and, as part of this, the use of novel experimental testing and

the related aerodynamic modelling techniques must be developed. Many unsteady and nonlinear aerodynamic effects due to flow separation can be spoiled or even totally missed due to inappropriate test conditions or aerodynamic data processing.

Flight tests with large scale controllable aircraft models dropped from a helicopter or aeroplane were effectively used in the past to complement wind tunnel tests in evaluating critical flight regimes such as stall and spin [2]. Recently there has been an increase in activity to develop experimental techniques for conducting virtual flight (or direct physical flight simulation) of an aircraft model in a wind tunnel working section. This approach is aimed at investigating the stability and control characteristics of the model with a view to extracting the aerodynamic data [3–7]. The idea is to allow an aircraft model to 'fly' in a wind tunnel working section with partially constrained motion imposed by a supporting system. The aircraft model has a number of degrees of freedom and this is expected to ensure more realistic aerodynamic loads than in captive (static and forced oscillation) testing, due to more natural model motion generated by deflections of control surfaces.

These techniques also potentially allow a significant reduction in aeroelastic coupling between an aircraft model and its support system compared with traditional dynamic testing. In static, forced oscillation and rotary balance tests, aircraft models are usually mounted on long cantilever stings through a strain gauge balance; such support systems are prone to sting-balance-model vibrations, which are especially strong under stall conditions due to coupling between unsteady separated flow and system elastic eigen modes [8, 9]. The excited vibrations of the sting-balance-model system have a considerable intrusive effect on the separated flow structure, changing measured aerodynamic loads [10]. A suitable virtual flight dynamic rig can be used to provide model motion measurements in different configurations with varying number of degrees of freedom, with reduced interaction with support structure dynamics (due to much lower eigen frequencies relative to conventional rigs), facilitating deeper insight into complicated unsteady and nonlinear aerodynamics strongly affected by separated flow conditions.

This paper presents experimental results obtained on the recently updated 5-DoF dynamic manoeuvre rig, developed at the University of Bristol [11–15] and now with improved actuation and data acquisition instrumentation. The tests were conducted in the University of Bristol $7' \times 5'$ (2.1m×1.5m) closed-section low-speed wind tunnel. A specially developed high-speed wireless message collection-distribution network allowed the distributed motion parameters to be recorded with synchronized time stamps in microseconds for phase-sensitive analysis; a low command-response loop latency (below ten milliseconds) made possible the implementation of real-time closed-loop feedback control strategies. Exploiting this new control capability, and specifically the feedback stabilisation, this paper reports on experiments that examine the aircraft model's nonlinear and unsteady aerodynamic characteristics, specifically for stall conditions. This is achieved through use of feedforward and feedback control strategies across a range of different combinations of the manoeuvre rig degrees of freedom. The results provide significant new insight into the cause of nonlinear limit cycle behaviour observed in previous test campaigns with the manoeuvre rig.

The updated manoeuvre rig and the aircraft model systems are briefly presented in Section II. The characteristics of post-stall self-sustained pitch oscillations of the aircraft model and their active control stabilization are detailed in Section III. The results of tests with one degree of freedom (model pitch) and two degrees of freedom (model pitch and rig arm pitch) are presented in Sections IV and V, respectively. And finally Section VI outlines results from tests with the manoeuvre rig in a four-DoF configuration with longitudinal and lateral-directional modes.

II. Manoeuvre Rig and Model Control System

The manoeuvre wind tunnel rig used in this study is shown schematically in Fig. 1a. An aircraft model is mounted on the arched end of the supporting sting on a 3-DoF gimbal giving the aircraft model freedom to move in pitch, yaw and roll within the following limits: $|\theta| \leq 20°$, $|\psi| \leq \infty$ and $|\phi| \leq 42°$ but diminishing to $\pm 15°$ as θ reaches its minimum or maximum values. The opposite, downstream, end of the sting is equipped with an aerodynamic compensator formed from four fins with deflectable trailing edge control surfaces. The sting, or rig arm, is mounted to a vertical support strut via a 3-DoF gimbal. Deflections of the rig arm in pitch θ_a and yaw ψ_a induce aircraft model movement in heave (up/down) and sway (left/right), respectively*. Essentially the aircraft model itself has 5 degrees of freedom because of the lack of a surge (fore/aft) DoF.

The first version of the manoeuvre rig was designed with a 2-DoF gimbal for the aircraft model [11, 12] but, aiming for simulation of asymmetrical departure at high angles of attack, the aircraft model had recently been equipped with a 3-DoF gimbal [15]. This allows simulation of rapid lateral departures. To avoid the aircraft model gimbal impacting its mechanical constraint during deflection in roll, the rig arm may be rotated to follow the aircraft model roll motions; this is achieved using feedback control driving the aerodynamic compensator on the rear of the rig arm [15].

The rig system is designed to be configured with different degrees of freedom by locking or releasing each axis or degree of freedom independently. The control surfaces on the four fins of the aerodynamic compensator mounted at the rear of the rig arm are primarily used for compensation of aerodynamic, inertial and gravitational forces generated on the rig arm but also can be used for forcing motion of the aircraft model in heave and sway.

The aircraft model used in this work – shown in Fig. 1b – is the same as in previous studies utilising the manoeuvre rig [12–15], namely an approximate replica of a $1/16^{th}$ scale BAe Hawk jet trainer aircraft model. The ailerons, elevator[†] and rudder are all actuated and can be used to control the aircraft model either manually via a stick input or using a command and stability augmentation control system via a ground station computer.

In addition to changes in mechanical design of the manoeuvre rig [15], recent enhancements include equipping the aircraft model and compensator surfaces with embedded microprogrammed control units for both sensing and actuating. To minimize mechanical friction from electrical wiring, the remote nodes use XBee Wi-Fi modules[16] for

---

*Note these motions are not precisely pure heave and sway as the aircraft is constrained to move in an arc.
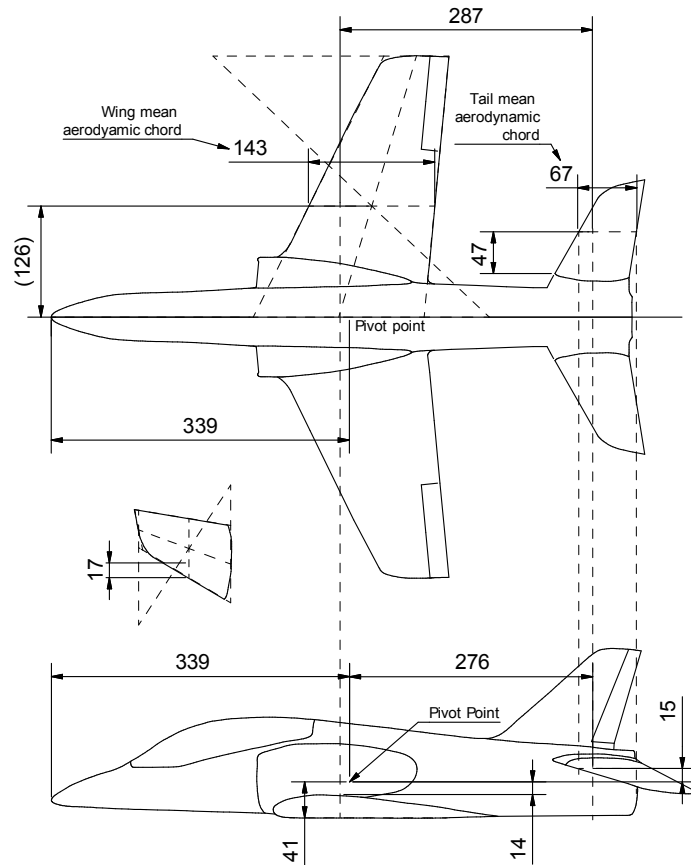[†]The model actually has an all-moving horizontal tail but it is referred to in this paper as an elevator.
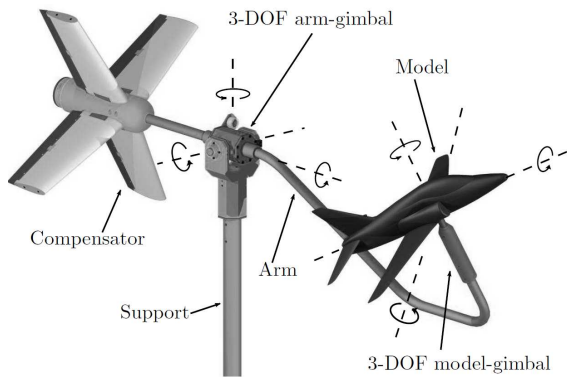
(a) Schematic diagram of rig.
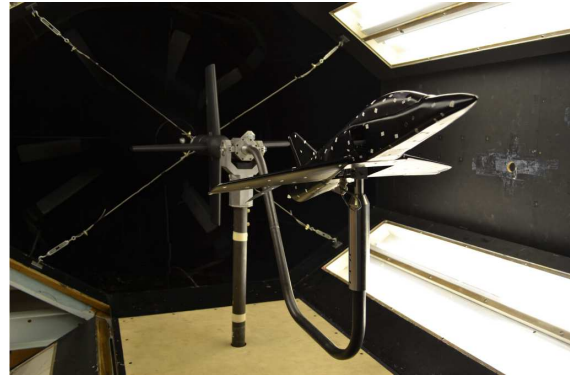
(b) Aircraft pitch-only configuration in $7' \times 5'$ closed section wind tunnel.

(c) Model geometry (dimensions in mm).

Fig. 1   The manoeuvre rig and aircraft model.

wireless communication with the ground station computer (or PC node). A distributed message delivery system runs on a real-time operating system in a 1kHz task loop on each remote node, which synchronizes the local clock with the PC node by a simplified version of the Network Time Protocol [17]. A health monitoring program running on the PC shows that the clock offsets are within 200 microseconds and the time latency of the command-response loops is kept below ten milliseconds. These upgrades provide two important features, namely the ability to post-process records from distributed nodes with microsecond accuracy timestamps and to implement feedback control with a communication delay of less than 10 ms.

The data acquisition system has also been upgraded by improving the method by which the attitude of the aircraft model is observed. In the previous manoeuvre rig design, the encoders and potentiometers on the model and rig gimbals were used to measure the relative attitudes of aircraft model-to-arm and arm-to-wind tunnel flow. From these signals the absolute attitudes and c.g. position of the aircraft model were calculated. However, this setup is unable to account for any aeroelastic deformation of the arm. Comparative tests showed that the maximum measurement errors caused by the aeroelastic effects can exceed one degree in the aircraft model attitude. The lead/lag errors in phase angle are also significant. In the upgraded rig, the kinematic measurement has been supplemented by an inertial measurement unit located inside the aircraft model allowing a Kalman filter to be used to estimate the aircraft attitude relative to the wind tunnel flow while also correcting the gyro drift [18].

The servo-control loop design for the control surface deflections on both the aircraft model and the compensator have been improved in terms of both the response rate and accuracy. A tuned proportional-plus-derivative control law, based on the experimentally-identified linearised motor model, forms the linear part of the servo control loop. In addition to this a nonlinear inversion control law is used to minimize steady-state errors by compensating the hinge friction via a Coulomb-like friction model. The servo-control code was implemented in the real-time operating system to sample angles and actuate motors. The Digital Signal Processor engines in the microprogrammed control units have been used to implement a Butterworth filter and numerical difference calculations for angular rates. As a result, the servo deflection may be viewed as an approximately linear second-order component, modelled by a second-order transfer function with the natural frequency of 30 rad/s and damping ratio 0.8. The rate saturation for the aircraft model actuators is approximately $300°/s$. The closed-loop transfer function indicates that with the servo controller the lag in response to input commands is reduced to approximately 100 milliseconds.

III. Post-Stall Pitch Oscillations and Their Active Control Suppression

It was reported in a number of previous publications, for example [13], that this Hawk aircraft model exhibits self-excited Limit Cycle Oscillations (LCOs) in pitch motion when trimmed by the elevator to angles of attack in the post-stall region. Those studies were not able to provide convincing evidence of the flow mechanisms responsible for the onset of this phenomenon in the trimmed state. The development of LCOs, due to instability of the aircraft model,

7

significantly transforms the separated flow and aerodynamic loads: as a result, it is impossible to observe flow over the model and to measure aerodynamic loads in steady conditions with constant angle of attack. The active control approach allows the aircraft model to be stabilized, eliminating onset of large amplitude LCOs.

The manoeuvre rig in these tests was configured to allow aircraft pitch-only motion (i.e. a 1-DoF setup).

Fig. 2a shows the variation of pitch angle $\theta(t)$ of the aircraft model, obtained in the wind tunnel test using the upgraded manoeuvre rig. A slowly changing ramp-like elevator input was applied over a time interval of 450 seconds. During the model pitch-up motion the LCOs were excited at $\delta_e = -7°$ and disappeared at $\delta_e = -21°$ via a transition to a stable equilibrium state. One should note that the model equilibrium states are agitated due to the wind tunnel flow turbulence and aeroelastic vibrations of the rig arm. The trimmed states of the aircraft model have small amplitude stochastic oscillations around the equilibrium point. The averaged LCOs for a number of different elevator deflections are shown in Fig. 2b in the form of phase trajectories.

After reaching the maximum pitch angle $\theta = 26.5°$ the elevator reverses, generating pitch-down motion. During the slow decrease in the model pitch angle the stable equilibrium states exist until approximately $\delta_e = -16°$. At this elevator deflection the LCOs are excited and there is an abrupt increase in the response amplitude. The levels of oscillation after this transition are the same as in the LCOs observed in the pitch-up motion. With further pitch-down elevator deflection the LCOs disappear after a smooth decrease of the amplitude to zero at $\delta_e = -7°$: this is the same condition as for the LCOs onset in the pitch-up motion.

Fig. 3a sketches the bifurcation structure for equilibrium states (solid lines) and LCOs amplitude (square markers) vs elevator deflection, the transitions between different steady-state branches of the aircraft model behaviour are indicated by the vertical arrows. These steady-state solutions (solid lines for equilibria and square markers for LCOs) were experimentally observed in the wind tunnel (see Fig. 2a). The sketch in Fig. 3a also includes provisional unstable steady-states for equilibria, shown as the dashed line segment between $\delta_e = -7°$ and $\delta_e = -16°$. From topological considerations, one should expect that this segment of the equilibrium states has oscillatory instability. Fig. 3a also shows the provisional amplitudes for unstable LCOs, marked by hollow circles. Being topologically consistent, the presented bifurcation diagram in Fig. 3a explains the onset and structure of the hysteretic transitions between the LCOs and stable equilibrium states.

The elevator of the Hawk model has sufficient control power to suppress the LCOs in the pitch motion of the aircraft model. This was demonstrated in the previous studies with application of a stabilising feedback control law using the manoeuvre rig with significantly higher time delays in the sensor-controller-actuator chain that is now achievable.

In the current study with updated manoeuvre rig hardware/software characteristics (see previous section), the feedback control law for elevator deflection is of the form:

$$\delta_e = \delta_{e_d}(\alpha) + \frac{k_\theta s}{s + \omega}\theta + k_q q, \tag{1}$$
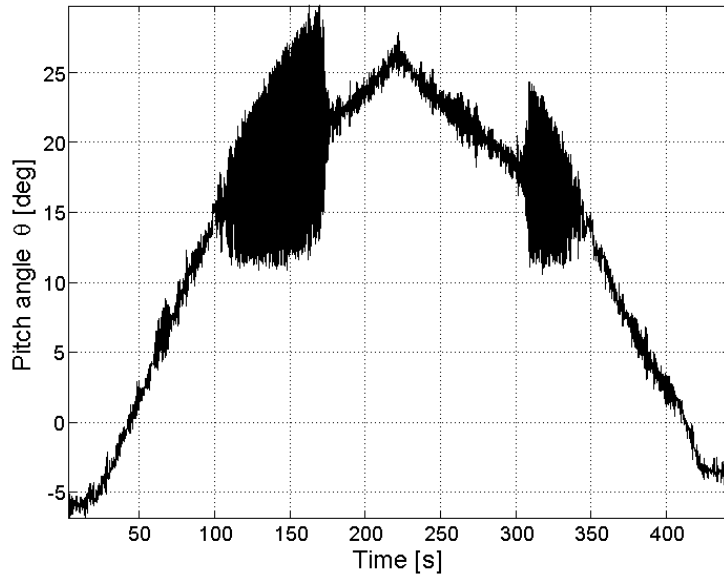
(a) Experimental record of the pitch angle variation vs elevator deflection.
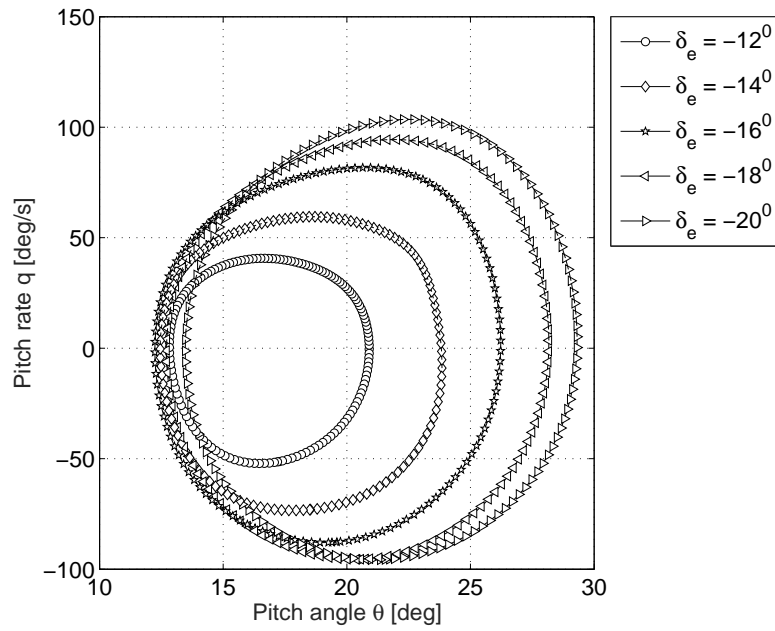
(b) Open loop LCOs at several elevator deflections.

Fig. 2   a) Measured response to slow pitch-up and -down elevator inputs and b) open loop LCOs.

where the values of k_q, k_θ, ω and $\delta_{e_d}(\alpha)$ are given in the Appendix. Pitch rate feedback was deployed to increase aircraft model damping, whilst the pitch angle was fed back to augment static stability and improve rejection of external disturbances from wind tunnel turbulence. The pitch angle $\theta(t)$ in (1) was obtained using the extended Kalman filter-based observer, while the pitch rate $q(t)$ is taken directly from the inertial gyro measurement unit and $\delta_{e_d}(t)$ is the elevator angle demand.

The gain coefficients k_θ and k_q in (1) were selected using iterative manual tuning on a linear mathematical model. This was constructed with aerodynamic characteristics estimated for the Hawk model at low angles of attack using steady state solutions of the Reynolds Averaged Navier-Stokes [19] equations. This aerodynamic analysis, based on CFD simulations in Fluent [20], was carried out by Bai Yalei at the Nanjing University of Aeronautics and Astronautics (NUAA), China.

The inclusion of the washout filter in (1) is to eliminate the influence of static offset in the pitch angle and so maintain a steady state elevator deflection equal to demand $\delta_e(\infty) = \delta_{e_d}$. Wind tunnel tests demonstrated that the feedback control law (1) stabilises the aircraft model equilibrium states in the stall region and at the same time eliminates the LCOs with low and large amplitudes at various elevator deflections δ_{e_d}.

Fig. 3b shows the effect the controller (1) has on the aircraft model pitch angle $\theta(t)$ time history for the experimental setup. Initially, the feedback controller is turned off with the elevator deflection set to $\delta_e = -16°$. At first, the aircraft model response is oscillatory with increasing amplitude around the unstable equilibrium state until the oscillations becomes fully developed – this takes about 2.5 seconds. The period of the developed LCO is approximately $T = 0.59\,\text{s}$ and the peak-to-peak amplitude is around $\Delta\theta \approx 13°$. The feedback controller (1) is switched on at $t = 468\,\text{s}$ with the control demand set to $\delta_{e_d} = -16°$. With the controller activated the pitch angle oscillations $\theta(t)$ converge within two seconds to the equilibrium state $\theta_e = 18°$ with an elevator deflection of $\delta_e = -16°$. This equilibrium state was unstable in the open loop system observed prior to $t = 468\,\text{s}$ – the controller has successfully suppressed the LCO by stabilising the equilibrium solution. In this equilibrium state the elevator actively compensates for disturbances from the wind tunnel turbulence and aeroelastic vibrations of the supporting rig arm giving rise to slight fluctuations in δ_e about $-16°$. The feedback control is switched off at $t = 475\,\text{s}$ and the aircraft model LCO reappears.

By testing at different command inputs over the range from $\delta_{e_d} = -5°$ to $\delta_{e_d} = -25°$ the controller (1) demonstrated its ability to suppress the large amplitude LCOs and to stabilise the equilibrium branch with only marginal oscillations in the elevator deflection required to mitigate against external disturbances.

IV. Pitch-Only Tests with Feedback Control to Track Stabilised Equilibrium States

Elimination of the large amplitude LCOs and stabilisation of the equilibrium states using the feedback controller (1) allows one to get an insight into possible equilibrium states, which are not observable in the aircraft model without stabilising feedback elevator control. An investigation of the stabilised equilibrium states at different elevator deflections
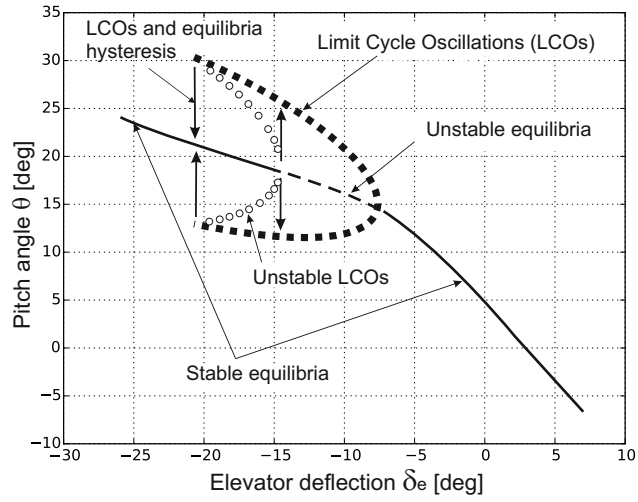
(a) Sketch of bifurcation structure.
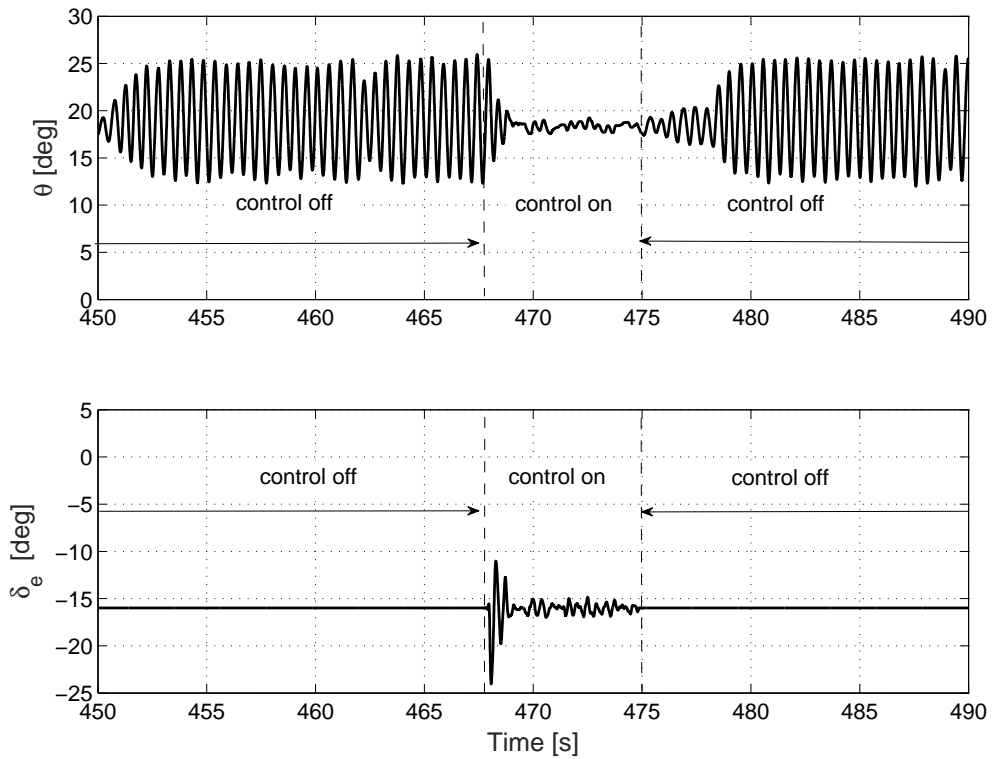
(b) Active suppression of LCOs using feedback control.

Fig. 3   a) Sketch of bifurcation diagram for equilibrium and LCOs and b) suppression of the LCOs using controller (1).
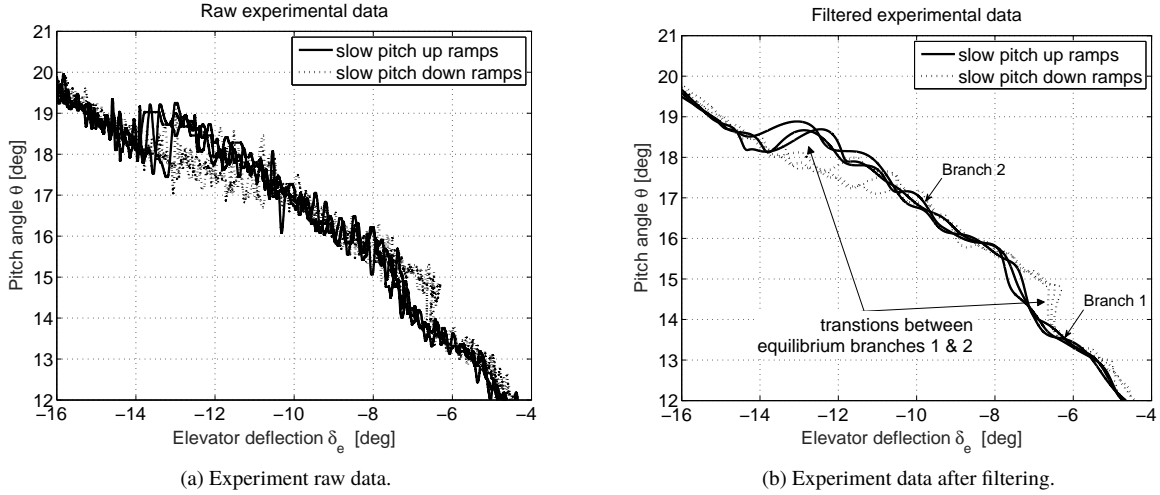
Fig. 4 **Trimmed pitch angle θ for slow pitch-up and -down elevator deflections with stabilising controller (1).**

and their dependence on previous motion within the stall region is now possible in the closed-loop system.

Such tests, with the elevator demand δ_{e_d} in the stabilising controller (1) set to a slowly varying ramp with $\dot{\delta}_{e_d} = \pm 0.2°/s$, were conducted on the rig configured for 1-DOF in pitch angle for the aircraft model. Fig. 4 shows the time histories for the aircraft model pitch angle $\theta(t)$ at slow pitch-up/pitch-down motions in the stall range of pitch angle $\theta \in [13°, 20°]$. The loops have been repeated three times. The solid lines depict the ramp motions with increasing incidence and the dotted lines depict the ramp motions with decreasing incidence. The stabilised pitch angles of the aircraft model in all the tests shown in Fig. 4a are quite noisy due to turbulence and rig arm vibrations. This noise blurs the subtle transitions in the pitch angle between different equilibrium branches. A Butterworth filter with a cutoff frequency of 0.2 Hz was used to reduce the effects of noise and smooth the raw data for the model pitch angle $\theta(t)$. Each curve is processed twice, once forward and once backwards in time, to retain zero phase delay. After such filtering the experimental curves became smoother and the pitch angle variations during elevator increase and decrease can be now distinguished from each other in Fig. 4b. The filtered experimental curves clearly show two zones of static hysteresis with transitions between different equilibrium branches. The first hysteresis loop is located in the range of pitch angle $\theta \approx 14° - 15°$ and the second, wider, hysteresis loop is located over $\theta \approx 17° - 19°$.

The equilibrium states provisionally shown in Fig. 3a can now be clarified. Fig. 5 shows the stabilised equilibrium branches, observed experimentally using the actively controlled aircraft model, along with the amplitudes of LCOs observed in the open-loop experiments and presented in Fig. 3a. Non-typical aerodynamic responses with abrupt jumps can be effectively interpreted based on generic topological properties manifested in nonlinear dynamical systems. The two static hysteresis regions between the equilibrium branches in Fig. 5 indicate bifurcational transitions between the equilibria solution branch at low and high α and a raised equilibrium branch in the range $\delta_e = -14°$ to $-7°$; this segment of equilibrium solutions is presumed to belong to the branches connected by fold bifurcations (with associated unstable

equilibria connecting the segments).

The Hawk model in this test is only free in the longitudinal mode while the lateral-directional degrees of freedom are fixed. The bifurcational changes in pitch angle can be triggered by changes in the flow structure which may be either symmetric or asymmetric in nature. Flow separation is highly sensitive to small geometric asymmetries of the Hawk model and this makes the onset of asymmetric separated flow conditions more probable. The verification of such an assumption in this case is presented in section VI.

The local angles of attack for the horizontal tailplane of the Hawk model remain low throughout the whole range of trim states considered, which ensures sufficient aerodynamic efficiency for active control stabilisation of the unstable equilibrium solutions; it also supports the conclusion that all nonlinear aerodynamic effects are localized on the wing.
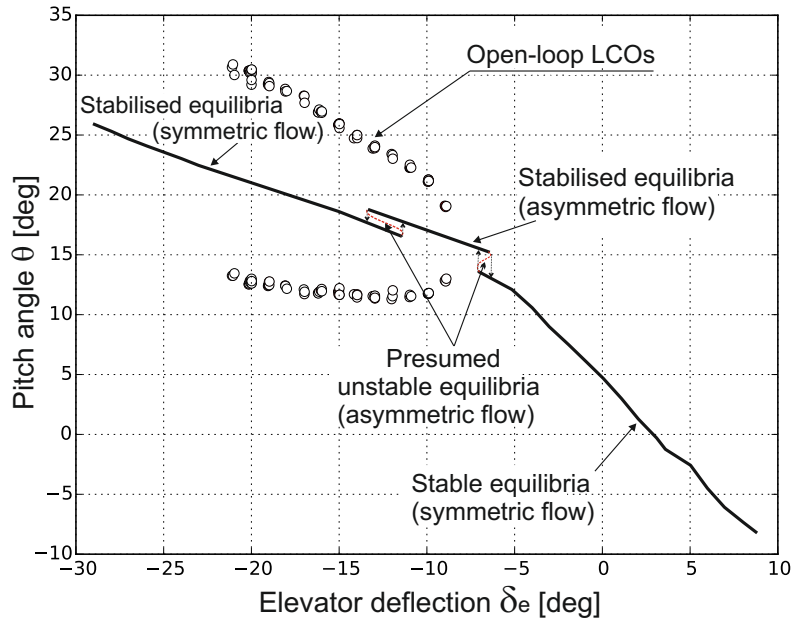

Fig. 5   Open-loop LCOs and stabilised equilibrium branches for aircraft model pitch-only configuration.

V. Heave-and-Pitch Tests with Active Stabilization of Equilibrium States

The test results shown in Fig. 5 demonstrate the nonlinear and bifurcational dependence of the pitch angle θ on the aircraft model elevator deflection δ_e, indicating existence of singularities in the pitching moment coefficient C_m. In the stall region one can expect more pronounced nonlinearities in the aerodynamic force dependence.

The version of the manoeuvre rig used here does not allow direct measurements of the aerodynamic loads using a traditional strain gauge balance or load cell. However, its design allows the aerodynamic force on the aircraft model to be measured indirectly using the heave-and-pitch rig configuration. In this configuration both the rig arm and the
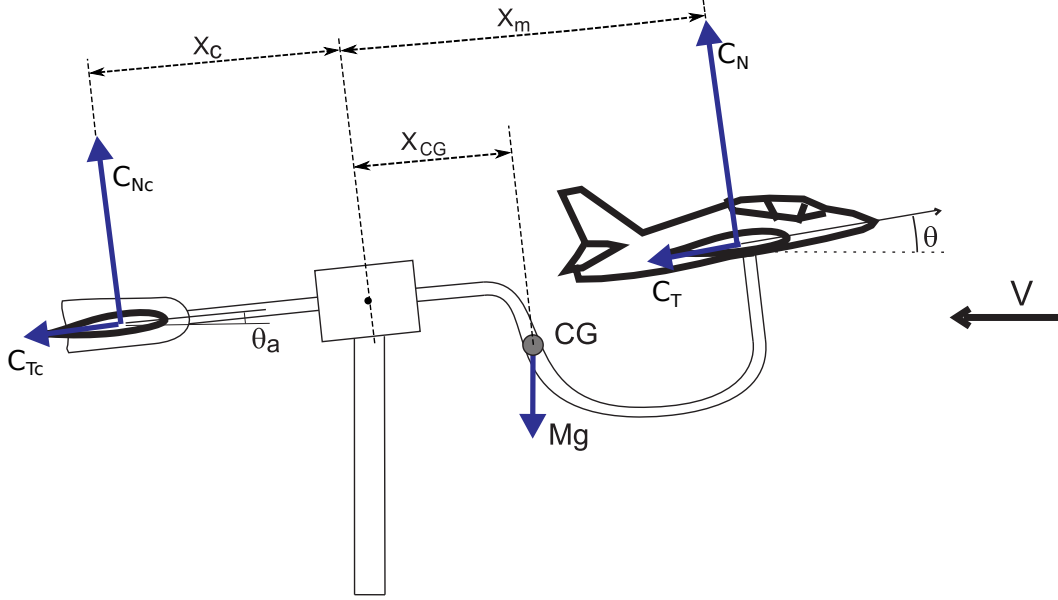
13

Fig. 6 Manoeuvre rig in heave-pitch 2-DoF configuration.

aircraft model are free to move in pitch with angles θ_a and θ respectively. The trim pitch angle of the aircraft model depends only on the aircraft model elevator δ_e while the trim pitch angle for the rig arm depends on δ_e and the elevator deflection for the aerodynamic compensator, δ_{ec}. Pitch-up and pitch-down ramp motions of the aircraft model were implemented using slow ramp inputs in aircraft elevator deflection δ_e similar to the tests presented in the previous section. In addition, the compensator elevators were used to stabilize the combined dynamics of the rig arm and the aircraft model to prevent the onset of the self-sustained LCOs.

With the rig arm free in pitch, it behaves as a mechanical balance scale. At every attitude of the aircraft model the arm will find an equilibrium position when the aerodynamic force of the aircraft model will be compensated by the aerodynamic force acting on the compensator (see Fig. 6). A simplified moment balance equation, accounting for the aircraft model aerodynamic forces (assumed to act at the aircraft gimbal centre), compensator aerodynamic forces (assumed to act at the compensator quarter-mean-aerodynamic-chord position) and the gravitational force due to the combined model and rig, about the vertical supporting strut gimbal is given by:

$$\bar{q} S C_N \cdot X_m = \bar{q} S_c C_{Nc} \cdot X_c + Mg \left\{ \cos(\theta_a) \cdot X_{CG} + \sin(\theta_a) \cdot Z_{CG} \right\}, \tag{2}$$

where

$$C_N = C_L \cos(\theta_a) + C_D \sin(\theta_a), \ \ C_{Nc} = C_{L_c} \cos(\theta_a) + C_{D_c} \sin(\theta_a), \tag{3}$$

and $C_L\,(\theta, \delta_e)$, $C_D\,(\theta, \delta_e)$, X_m and S_m are the aircraft model aerodynamic lift and drag coefficients, normal-force moment arm to the vertical strut gimbal and wing area respectively. Also $C_{L_c}\,(\theta_a, \delta_{ec})$, $C_{D_c}\,(\theta_a, \delta_{ec})$, X_c and S_c are the

compensator aerodynamic lift and drag coefficients, the normal-force moment arm and the compensator aerodynamic area respectively; M, X_{CG} and Z_{CG} are the effective mass and centre-of-gravity location for the rig arm, compensator and aircraft model combined.

The rig is configured (in terms of mass and CG location) such that the trim conditions are realised at low arm pitch angles θ_a, where flow on the compensator is attached and the lift force C_{L_c} can be presented as a linear function of the pitch angle θ_a. Equation (2) can then be written:

$$C_N\left(\theta, \delta_e\right) = \frac{S_c X_c}{S X_m}\left(C_{Nc_{\theta_a}}\theta_a + C_{Nc_{\delta_{ec}}}\delta_{ec}\right) + \frac{Mg\left\{\cos(\theta_a)\cdot X_{CG} + \sin(\theta_a)\cdot Z_{CG}\right\}}{\bar{q}SX_m}. \tag{4}$$

Using the small-angle approximations, $\cos\theta_a = 1$ and $\sin\theta_a = \theta_a$, this becomes:

$$C_N\left(\theta, \delta_e\right) \approx \left(\frac{S_c X_c C_{Nc_{\theta_a}}}{S X_m} + \frac{Mg Z_{CG}}{\bar{q}SX_m}\right)\theta_a + \left(\frac{S_c X_c C_{Nc_{\delta_{ec}}}}{S X_m}\delta_{ec} + \frac{Mg X_{CG}}{\bar{q}SX_m}\right) \tag{5}$$

Thus the aerodynamic normal force coefficient, C_N, can be considered to have a linear dependence on the arm pitch angle, θ_a.

In the tests with the heave-and-pitch rig configuration (Fig. 6) the aircraft model was trimmed and stabilised by the aircraft model elevator δ_e using the feeback control law (1). The rig arm was controlled and stabilised using compensator elevator δ_{ec} by feeding back the arm pitch rate signal q_a to increase the damping of the aircraft model heave movement, while retaining the same trimmed states:

$$\delta_e = \delta_{e_d} + \frac{k_\theta s}{s+\omega}\theta + k_q q,$$
$$\delta_{ec} = \delta_{ec_d} + k_{q_a}q_a. \tag{6}$$

Fig. 7a presents the experimental data for trim angles θ_a (the rig arm attitude) versus trim angles θ (the aircraft model attitude). Note that in trim conditions the pitch angle equals the aircraft model angle of attack ($\theta = \alpha$). Two sets of slow pitch-up (solid lines) and slow pitch-down (dotted lines) ramp movements were conducted by varying the aircraft model elevator demand $\delta_{e_d}(t)$ in a slow ramp while demanding zero compensator elevator deflection $\delta_{ec_d} = 0$.

The experimental data have been post-processed to remove any high frequency oscillatory component, arising from wind tunnel turbulence, model vibrations, etc. Assuming a small angle of attack and no stall on the aerodynamic compensator, the aerodynamic force on the aircraft model is approximately proportional to the arm pitch angle θ_a (4), so the curves shown in Fig. 7a can be viewed as representing the dependence of the aerodynamic force on the aircraft model on its pitch angle (or angle of attack). The aerodynamic normal force coefficient C_N can be calibrated experimentally against the arm pitch angle θ_a.

15

Two–DoF heave–pitch mode
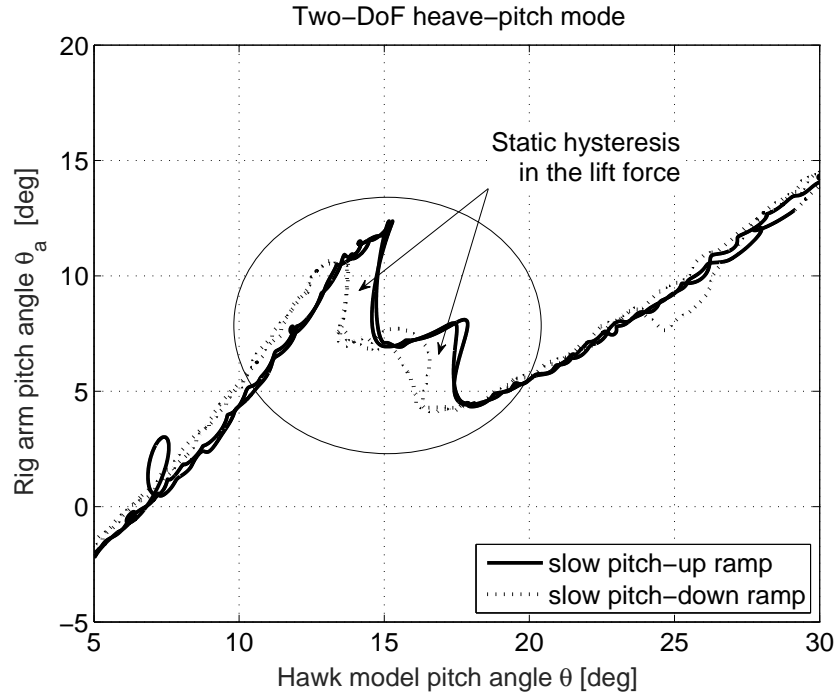
(a) Experimental measurments after filtering.
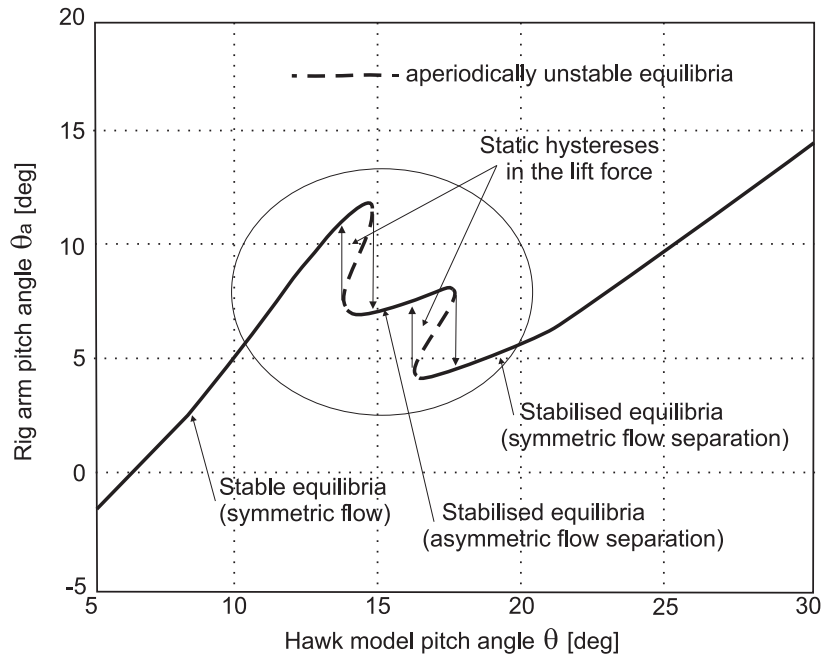
(b) Presumed bifurcation diagram for θ_a vs θ.

Fig. 7   **Actively stabilised trim states θ_a and θ on the heave-pitch rig configuration (Fig. 6).**

Considering in Fig. 7a the variation of rig arm attitude θ_a as model pitch angle θ increases: after a nearly linear increase in θ_a with θ, θ_a drops abruptly from $12°$ to $7°$ at $\theta = 15°$. Note that the model pitch angle is equal to the angle

of attack ($\alpha = \theta$). A further slight increase in θ_a takes place until $\theta_a = 8°$ at $\theta = 17.5°$. At this point a second abrupt

drop in arm pitch angle occurs from $\theta_a = 8°$ to $\theta_a = 4°$. Further increase in θ results in a further linear increase in θ_a

until $\theta_a = 14°$ at $\theta = 30°$. During slow reverse deflection of the aircraft model elevator ($\dot{\delta}_e > 0$) there are again two

vertical jumps but now with increases in the rig arm attitude. These both occur at roughly one degree lower model pitch

angle, or angle of attack, than the drops observed in the tests with increasing angle of attack. The abrupt transitions

in the experimentally measured rig arm attitude, θ_a, may be triggered by bifurcations in flow separation processes in

the stall region. Since the rig arm attitude relates directly to the lift coefficient dependence on angle of attack, $C_L(\alpha)$,

these bifurcations in flow structure are reflected in the force coefficient in a similar way, namely discontinuous jumps in

the aerodynamic force acting on the aircraft model during slow changes in angle of attack α. Similarly, the hysteretic

variations in model trim angle of attack exhibited in Figs. 4 and 5 are linked to the hysteretic dependence of the pitching

moment on angle of attack, $C_m(\alpha)$.

In interpreting the sudden jumps in the experimental data, an analogy with bifurcational models is useful. Fig. 7b

shows a hypothetical bifurcation diagram for stabilised equilibrium states θ_a and θ. It includes three stable branches

in θ_a dependence on pitch angle θ (recalling that in trimmed conditions $\theta = \alpha$). The intermediate branch, located in

the range of $\theta \approx 14° - 17.5°$, is identical to the intermediate branch identified earlier using 1-DoF tests on the aircraft

model in which only the aircraft pitch angle was free to move (see Fig. 5). All three stabilised equilibrium branches are

connected in so called saddle-node bifurcation points via hypothetically existing aperiodically unstable equilibrium

branches (dashed lines). Abrupt jumps occur at these bifurcation points if the pitch angle is swept past them, forming

the experimentally observed static hysteresis loops.

The cause of these abrupt transitions in the aircraft model equilibrium states is connected with topological changes in

the flow structure in the stall region. Transitions from attached to separated flow conditions and changes in structure of

separated flow may be reflected in the aerodynamic loads in the form of jump-like changes. As discussed in Section IV,

evidence suggests that the first transition towards the intermediate branch may correspond to the onset of asymmetric

separated flow conditions, which exist in a narrow range of angles of attack. The second transition towards the third

stabilised equilibrium branch is then assumed to be linked to symmetrization of the separated flow structure. These

assumptions are examined further in the next section with the rig operating in four DoF (heave-pitch-roll-yaw) to include

lateral-directional effects.

VI. 4-DoF Coupled Longitudinal and Lateral-Directional Tests

In order to improve insight into the observed aerodynamic hysteresis of the aircraft model, tests were conducted with

the aircraft gimbal unlocked in all three DoF's (roll, pitch and yaw) and the arm free to move in pitch to approximate

aircraft heave motion. The aim was to identify whether lateral-directional aerodynamic moments are generated along

with the bifurcational aerodynamic dependencies in the longitudinal dynamics. This rig configuration allows the aircraft

model to move in roll and yaw degrees of freedom, facilitating the testing of possible onset of asymmetric aerodynamic moments. Many aircraft configurations at high angles of attack manifest so-called 'wing rock' oscillations due to the local instability of the Dutch roll mode and nonlinear dependence of aerodynamic moments on sideslip and velocity roll rate. The local instability in the lateral-directional modes can be stabilized using ailerons and rudder via feedback signals proportional to roll and yaw rates. Appearance of asymmetric aerodynamic moments will be indicated in the experiments by non-zero roll and yaw trim angles.

In the selected configuration, to allow stabilisation of equilibrium states and elimination of the wing rock regime, a simple controller was implemented utilising roll and yaw angle and angular rates feedback to the ailerons (δ_a) and rudder (δ_r). This is combined with the previously described longitudinal control using the aircraft model elevator and the aerodynamic compensator:

$$\delta_e = \delta_{e_d} + \frac{k_\theta s}{s+\omega}\theta + k_q q,$$

$$\delta_{ec} = \delta_{ec_d} + k_{q_a} q_a,$$

$$\delta_a = \delta_{a_d} + k_\phi \phi + k_p p, \tag{7}$$

$$\delta_r = \delta_{r_d} + \frac{k_\psi s}{s+\omega}\psi + k_r r,$$

where feedback gains k_ϕ and k_ψ augment aerodynamic stiffness in the roll and yaw deflections respectively. The feedback gains k_ϕ and k_ψ were selected with the objective of preventing rotation and limiting the trimmed angles in roll and yaw caused by asymmetric aerodynamical rolling and yawing moments. Feedback gains k_p and k_r are used to stabilise the lateral-directional modes and supress wing rock oscillations. Values adopted for these gains are presented in the Appendix.

To evaluate the aircraft model roll and yaw angles at trim conditions the following representation of the rolling and yawing aerodynamic moments are considered:

$$C_l = C_{l_0}(\alpha) + C_{l_\beta}(\alpha)\beta + C_{l_p}(\alpha)\frac{pb}{2V} + C_{l_r}(\alpha)\frac{rb}{2V} + C_{l_{\delta_a}}(\alpha)\delta_a + C_{l_{\delta_r}}(\alpha)\delta_r,$$

$$\tag{8}$$

$$C_n = C_{n_0}(\alpha) + C_{n_\beta}(\alpha)\beta + C_{n_p}(\alpha)\frac{pb}{2V} + C_{n_r}(\alpha)\frac{rb}{2V} + C_{n_{\delta_a}}(\alpha)\delta_a + C_{n_{\delta_r}}(\alpha)\delta_r.$$

The attitude angles θ, ϕ and ψ for the aircraft model, mounted on the 3-DoF gimbal, in trim conditions are related to

18

the angle of attack α and sideslip β. For small roll and yaw angles the following simplified relations can be used:

$$\phi \ll 1, \psi \ll 1,$$

$$\alpha = \theta; \beta = \phi \sin \alpha + \psi.$$

(9)

The trim roll and yaw angles (ϕ_s and ψ_s, respectively) are determined according to (7), (8) and (9) under zero rotation conditions ($p = r = 0$):

$$\phi_s = \frac{\triangle C_l(\alpha)C_{n_\beta}(\alpha) - \triangle C_n(\alpha)C_{l_\beta}(\alpha)}{k_\phi \left(C_{l_{\delta_a}}(\alpha)C_{n_\beta}(\alpha) - C_{n_{\delta_a}}(\alpha)C_{l_\beta}(\alpha)\right)}$$

$$\psi_s = \frac{-\triangle C_n(\alpha)\left(C_{l_\beta}(\alpha)\sin\alpha + k_\phi C_{l_{\delta_a}}(\alpha)\right) + \triangle C_l(\alpha)\left(C_{n_\beta}(\alpha)\sin\alpha + k_\phi C_{n_{\delta_a}}(\alpha)\right)}{k_\phi \left(C_{l_{\delta_a}}(\alpha)C_{n_\beta}(\alpha) - C_{n_{\delta_a}}(\alpha)C_{l_\beta}(\alpha)\right)}$$

(10)

where

$$\triangle C_l(\alpha) = C_{l_0}(\alpha) + C_{l_{\delta_a}}(\alpha)\delta_{a_d} + C_{l_{\delta_r}}(\alpha)\delta_{r_d} \quad \text{and} \quad \triangle C_n(\alpha) = C_{n_0}(\alpha) + C_{n_{\delta_a}}(\alpha)\delta_{a_d} + C_{n_{\delta_r}}(\alpha)\delta_{r_d}.$$ (11)

In the case of no asymmetric aerodynamic moments, $C_{l_0} = C_{n_0} = 0$ and with zero commanded control inputs, $\delta_{a_d} = \delta_{r_d} = 0$, the aircraft model roll and yaw angles (10) should be zero. Therefore the trim angles ϕ_s and ψ_s can serve as a measure of asymmetry in the aerodynamic moments, when $\delta_{a_d} = \delta_{r_d} \approx 0$.

Figs. 8a and 8b show the filtered values for quasi-static roll and yaw angles, $\phi_s(t)$ and $\psi_s(t)$ respectively, obtained using the manoeuvre rig with the aircraft pitch, roll and yaw degrees of freedom released in addition to the arm pitch angle (which approximates aircraft heave). Tests in which the elevator deflection was slowly ramped up and down (with $|\dot{\delta}_{e_d}| \ll 1°/$s) were conducted. In these runs, command inputs to the controllers were $\delta_{a_d} = 0$ and $\delta_{r_d} = 0$ and the gain k_ψ was set to zero. Figs. 8c and 8d show similar processes for the case when the rudder demand was non-zero, using $\delta_{a_d} = 0$ and $\delta_{r_d} = \pm 10°$.

At low angles of attack and attached flow conditions ($\alpha = -5°$ to $13°$) the trim angles in roll and yaw shown in Figs. 8a and 8b are quite small ($\phi_s \approx -2°$, $\psi_s \approx 1°$). These asymmetric trim angles are probably associated with small imperfections in the aircraft model geometry, which trigger a massive asymmetric flow separation and significantly increase magnitudes of trim angles ϕ_s and ψ_s in the range $\alpha = 14°$ to $17.5°$. At higher angles of attack, $\alpha > 17°$, the level of asymmetric aerodynamic moments reduces to that at low incidences. With further increase in angle of attack, $\alpha > 20°$, asymmetry in the yaw moment becomes more prominent. Therefore the experimental results shown in Fig. 8 also indicate the existence of the hysteretic dependencies in the asymmetric aerodynamic loads.

The aerodynamic asymmetry detected in the tests on the manoeuvre rig with heave, pitch, roll and yaw degrees
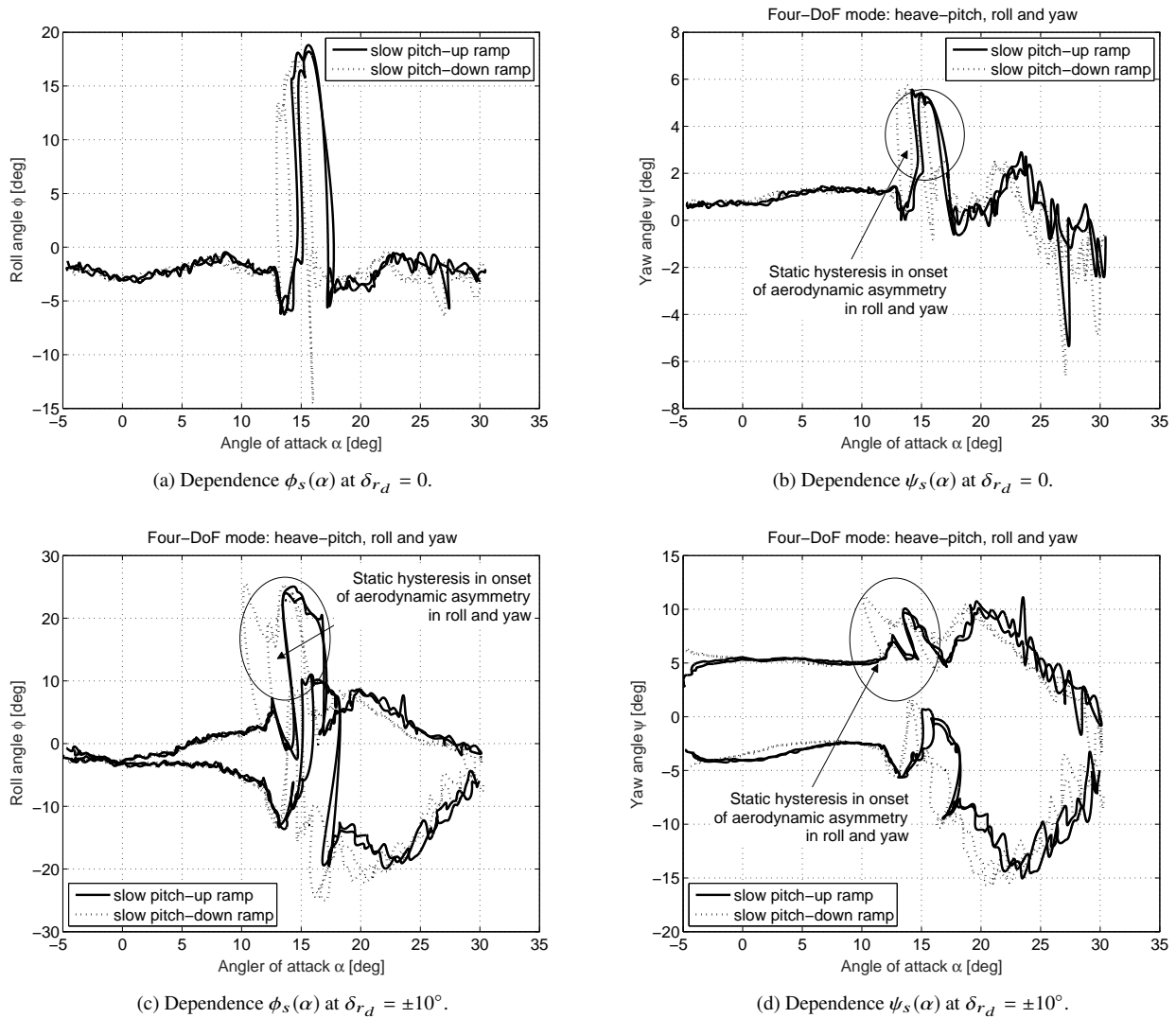
(a) Dependence $\phi_s(\alpha)$ at $\delta_{r_d} = 0$.

(b) Dependence $\psi_s(\alpha)$ at $\delta_{r_d} = 0$.

(c) Dependence $\phi_s(\alpha)$ at $\delta_{r_d} = \pm 10°$.

(d) Dependence $\psi_s(\alpha)$ at $\delta_{r_d} = \pm 10°$.

Fig. 8   Stabilised trim angles ϕ_s and ψ_s with model free in heave, pitch, roll and yaw.

of freedom is located in the range of angle of attack $\alpha = 14°$ to $17.5°$, which matches well with the location of the intermediate equilibrium branches in the presumed bifurcation diagrams shown in Figs. 4 and 7b. The onset of this massive aerodynamic asymmetry in the rolling (C_{l_0}) and yawing (C_{n_0}) moments has a distinct hysteretic dependence in the pitch-up (solid lines) and pitch-down (dashed lines in Fig. 7b) ramp motions with an angle of attack shift of $\triangle\alpha \approx \pm 2°$. This corresponds closely with the earlier test results obtained with the rig configured as pitch-only and with heave-and-pitch degrees of freedom. These observations clearly show that asymmetric flow separation phenomena are an important feature shaping the aerodynamic loads in the stall region of the tested Hawk model.

VII. Concluding Remarks

The paper presents the results of an experimental study of stall aerodynamics via stabilization of unstable trim states of an approximate copy of a 1/16th-scale Hawk aircraft model. The tests have been conducted using the updated University of Bristol multi-degree-of-freedom manoeuvre rig in a low-speed wind tunnel. The aircraft model is attached via a 3-DoF gimbal to an arm which itself is free to move in up to three DoFs about a point set back from the model such that approximate vertical and horizontal translational motion of the model can be simulated. In addition to the experimental results, this paper presents the improvements in hardware and communication systems implemented in the experimental rig.

The experimental rig has a number of advantages compared with traditional static and dynamic testing apparatus. The rig can be configured to allow the Hawk model to be free in pitch, plunge, roll and yaw in different combinations and allows a significant reduction in aeroelastic coupling between an aircraft model and its support system compared with traditional static and dynamic testing. Note that in traditional testing, when the aircraft model is firmly fixed on a sting with a strain gauge balance, flow instability and aerodynamic buffet in the stall region excite structural vibrations of the support sting; this has a considerable intrusive effect on the separated flow structure, affecting measured aerodynamic loads. Possible hysteretic dependencies in static conditions may be significantly transformed and effectively linearized, so that aerodynamics loads show only single discontinuous or steep changes. Structural dynamic effects on the manoeuvre rig as well as on traditional model-fixed testing facilities require further investigation.

The rig compensator and the Hawk model have actuated aerodynamic control surfaces which are used for trimming the aircraft model and stabilization of its unstable equilibria. These control surfaces are operated in attached flow conditions and are regarded as linear control effectors. Their influence on the flow around the Hawk model is assumed in this work to be small.

The dynamic rig with active stabilization of unstable modes of the freely moving model allows deeper insight into stall aerodynamics. The obtained experimental results clearly show the existence of hysteresis phenomena with abrupt jumps between different branches in the dependencies of the normal aerodynamic force observed in static stall conditions. Qualitative bifurcation analysis of the measured aerodynamic dependencies at zero sideslip indicates that the intermediate branch of the aerodynamic hysteresis, in some range of angles of attack, is associated with the onset of asymmetric rolling and yawing aerodynamic moments due to an asymmetric separated flow structure. The observed static hysteresis phenomena prove that the proposed concept of testing is opening new opportunities in experimental testing of stall aerodynamics, helping to identify possible causes of the onset of LCOs.

The measured static aerodynamic hysteresis demonstrates the expanded capabilities of the updated and actively controlled wind tunnel manoeuvre rig with improved hardware and communication software. In addition to facilitating physical simulations of the aircraft model dynamics at stall conditions, it serves as a minimally-intrusive system — minimising the coupling of support system structural dynamics with the unsteady flow dynamics — for investigation of

separated flow conditions by experimental continuation of stabilised aircraft model trim states. The advantages delivered by this actively controlled testing approach make it a valuable complement to traditional wind tunnel test techniques.

The findings in this paper suggest promising prospects for the multi-DOF testing methodology. Thorough comparisons with other experimental methods are needed, and further computational and experimental studies are required in order to gain a comprehensive understanding of unsteady nonlinear aerodynamic phenomena in the stall region.

Acknowledgements

References

[1] Cooperative Programme on Dynamic Wind Tunnel Experiments for Manoeuvrable Aircraft, AGARD-AR-305, 1996.

[2] CHAMBERS, J.R. Modeling Flight: The Role of Dynamically Scaled Free-Flight Models in Support of NASA's Aerospace Programs, *NASA SP 2009-575*, 2009. ISBN: 978-0-16-084633-5.

[3] OWENS, D.B., BRANDON, J.M., CROOM, M.A., FREMAUX, C.M., HEIM, E.H. and VICROY, D.D. Overview of Dynamic Test Techniques for Flight Dynamics Research at NASA LaRC, *25th AIAA Aerodynamic Measurement Technology & Ground Testing Conference*, San Francisco CA, 2006, AIAA-2006-3146. doi: 10.2514/6.2006-3146.

[4] HUANG, M. and WANG, Z.-W. A Review of Wind Tunnel Based Virtual Flight Testing Techniques for Evaluation of Flight Control Systems *International Journal of Aerospace Engineering*, 2015, Article ID 672423. doi: 10.1155/2015/672423.

[5] IGNATYEV, D.I., SIDORYUK, M.E., KOLINKO, K.A. and KHRABROV, A.N. Dynamic Rig for Validation of Control Algorithms at High Angles of Attack *Journal of Aircraft*, 2017, **54**, (5), pp 1760–1771. doi: 10.2514/1.C034167.

[6] LI, H., ZHAO, Z.-L. and FAN, Z.-L. Simulation Method for Wind Tunnel Based Virtual Flight Testing, *International Journal of Modern Physics: Conference Series*, 2012, **19**, pp 381–389. doi: 10.1142/S2010194512008975.

[7] MUSE, J.A., KUTAYY, A. and CALISE, A.J. A Novel Force Control Traverse for Simulating UAV Flight In A Wind Tunnel, *AIAA Atmospheric Flight Mechanics Conference & Exhibit*, Honolulu HI, 2008, AIAA-2008-6714. doi: 10.2514/6.2008-6714.

[8] CHEN, J., SHEN, X., TU, F. and QURESHI, E.M. Experimental Research on an Active Sting Damper in a Low Speed Acoustic Wind Tunnel, *Shock and Vibration, Hindawi Publishing Corporation*, Volume 2014, Article ID 524351, 10pp. doi: 10.1155/2014/524351.

[9] BALAKRISHNA, S., HOULDEN, H.,, BUTLER, D.H., and WHITE, R. Development of a wind tunnel active vibration reduction system, in *Collection of Technical Papers - 45th AIAA Aerospace Sciences Meeting and Exhibit*, Volume 17, Pages 11661-11672, Reno, Nev, USA, January 2007.

[10] YE, J.Z.,JIANG, Y.W.,ZHOU, N.Z.,SONG, B.F. and HE, Z.J. The aeroelastic effects on the scatter phenomenon of wind-tunnel data, *Science China Technological Sciences*, Volume 56, Issue 2, February 2013, pp 405-415. doi: 10.1007/s11431-012-5100-6.

[11] PATTINSON, J. Development and Evaluation of a Wind Tunnel Manoeuvre Rig, *PhD thesis*, University of Bristol, 2010.

[12] PATTINSON, J., LOWENBERG, M.H. and GOMAN, M.G. Multi-Degree-of-Freedom Wind-Tunnel Maneuver Rig for Dynamic Simulation and Aerodynamic Model Identification, *AIAA Journal of Aircraft*, 2012, **50**, (2), pp 551–566. doi: 10.2514/1.C031924.

[13] PATTINSON, J., LOWENBERG, M.H. and GOMAN, M.G. Investigation of Poststall Pitch Oscillations of an Aircraft Wind-Tunnel Model, *AIAA Journal of Aircraft*, 2013, **50**, (6), pp 1843–1855. doi: 10.2514/1.C032184.

[14] ARAUJO-ESTRADA, S.A., LOWENBERG, M., NEILD, S. and GOMAN, M. Evaluation of Aircraft Model Upset Behaviour Using Wind Tunnel Manoeuvre Rig, *AIAA Atmospheric Flight Mechanics Conference*, Kissimmee FL, 2015, AIAA-2015-0750. doi: 10.2514/6.2015-0750.

[15] ARAUJO-ESTRADA, S.A., GONG, Z., LOWENBERG, M., NEILD, S. and GOMAN, M. Wind Tunnel Manoeuvre Rig: A Multi-DOF and HAOA Testing Platform for Model Aircraft, *AIAA Science and Technology Forum & Exposition*, San Diego CA, 2016, AIAA-2016-2119. doi: 10.2514/6.2016-2119.

[16] DIGI.COM. XBee Wi-Fi, http://www.digi.com/products/xbee-rf-solutions/modules/xbee-wi-fi, [Online; accessed 14-December-2015].

[17] MILLS, D.L. Network time protocol version 4 reference and implementation guide, *Network Time Protocol Working Group*, University of Delaware 2006, report 06-6-1.

[18] CARNDUFF, S., ERBSLOEH, S., COOKE, A. and COOK, M. Development of a low cost dynamic wind tunnel facility utilizing MEMS inertial sensors, *46th AIAA Aerospace Sciences Meeting & Exhibit*, Reno NV, 2008, AIAA-2008-196.

[19] VERSTEEG, H.K. AND MALALASEKERA, W. An Introduction to Computation Fluid Dynamics: the Finite Volume Method, 2nd ed. *Pearson*, 2007. ISBN: 978-0-13-127498-3.

[20] ANON. ANSYS Fluent User's Guide, release 16.2, *ANSYS, Canonsburg, PA, USA*, 2015.

23

Appendix

Table A1 Hawk model, compensator and rig characteristics.

Quantity	Aircraft model	Compensator	Rig arm
Mass	1.97 kg	3.91 kg	3.65 kg
Position of CG ahead of arm gimbal centre, $\theta_a = 0$	0.80 m	−0.38 m	0.262 m
Position of CG below arm gimbal centre, $\theta_a = 0$	0	0	0.109 m
Reference area	0.0796 m^2	0.125 m^2	
Mean aerodynamic chord	0.143 m	0.181 m	
1/4-chord sweep	21.7°	7.12°	
Span	0.594 m	0.700 m	
Moment of inertia about x body axis	8.08×10^{-3} kgm^2		
Moment of inertia about y body axis	4.76×10^{-2} kgm^2		
Moment of inertia about x body axis	6.12×10^{-2} kgm^2		

Table A2 Mass and CG position of combined rig/Hawk model/compensator.

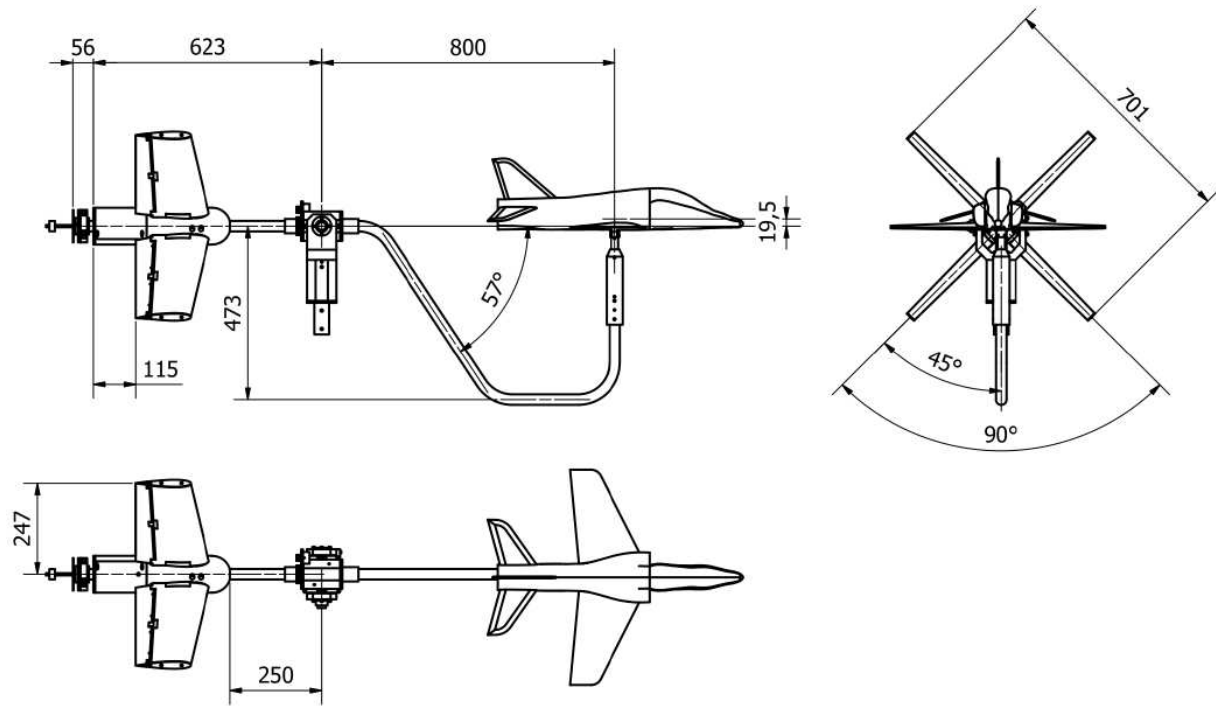|	
Mass, M	9.53 kg
Position of CG ahead of arm gimbal centre, X_{CG}	0.109 m
Position of CG below arm gimbal centre, Z_{CG}	0.0417 m

Fig. A1   Rig dimensions.

Table A3   Controller constants.

Quantity	Unit	Eqn. (1)	Eqn. (6)	Eqn. (7)
k_q	s	0.28	0.28	0.28
k_θ	–	0.60	0.60	0.60
ω	rad/s	0.20	0.20	0.20
k_{q_a}	s		1.0	1.0
k_ϕ	–			0.40
k_p	s			0.10
k_ψ	–			2.0
k_r	s			1.0

Table A4   Data for δ_{e_d} as a function of trimmed α.

α (°)	-8.0991	–6.3681	–4.3233	–2.9083	–1.4130	–0.075879	1.8904	4.0136
δ_{e_d} (°)	8.6826	7.0658	5.8084	5.4491	3.8323	2.9341	1.6767	0.59880
α (°)	5.9801	7.9466	9.5986	11.879	12.824	14.634	16.700	17.000
δ_{e_d} (°)	–0.83832	–2.2755	–3.5329	–4.9701	–6.4072	–7.6647	–11.000	–13.144
α (°)	18.652	19.912	20.938	22.276	23.222	24.561	25.820	
δ_{e_d} (°)	–15.928	–18.084	–20.778	–22.755	–24.910	–27.156	–29.132	